Environmental Pollution 329 (2023) 121656

Contents lists available at ScienceDirect

Environmental Pollution

journal homepage: www.elsevier.com/locate/envpol

The potential effects of *in vitro* digestion on the physicochemical and biological characteristics of polystyrene nanoplastics☆

Lourdes Vela [a,b], Aliro Villacorta [a,c], Tom Venus [d], Irina Estrela-Lopis [d], Susana Pastor [a], Alba García-Rodriguez [a], Laura Rubio [a,e], Ricard Marcos [a,*], Alba Hernández [a]

[a] Group of Mutagenesis, Department of Genetics and Microbiology, Faculty of Biosciences, Universitat Autònoma de Barcelona, Cerdanyola Del Vallès, Spain
[b] Facultad de Ciencias de La Salud, Eugenio Espejo. Universidad UTE, Avenida Occidental y Mariana de Jesús, Quito, Ecuador
[c] Facultad de Recursos Naturales Renovables, Universidad Arturo Prat, Iquique, Chile
[d] Institute of Medical Physics and Biophysics, University of Leipzig, 04107, Leipzig, Germany
[e] Nanobiology Laboratory, Department of Natural and Exact Sciences, Pontificia Universidad Católica Madre y Maestra, PUCMM, Santiago de Los Caballeros, Dominican Republic

ARTICLE INFO

Keywords:
Nanoplastics
Polystyrene
Digestion
Characterization
Cell uptake
Hazard effects

ABSTRACT

The presence of plastic waste in our environment has continued growing and become an important environmental concern. Because of its degradation into micro- and nanoplastics (MNPLs), MNPLs are becoming environmental pollutants of special environmental/health concern. Since ingestion is one of the main exposure routes to MNPLs, the potential effects of digestion on the physicochemical/biological characteristics of polystyrene nanoplastics (PSNPLs) were determined. The results indicated a high tendency of digested PSNPLs to agglomerate and a differential presence of proteins on their surface. Interestingly, digested PSNPLs showed greater cell uptake than undigested PSNPLs in all three tested cell lines (TK6, Raji-B, and THP-1). Despite these differences in cell uptake, no differences in toxicity were observed except for high and assumed unrealistic exposures. When oxidative stress and genotoxicity induction were determined, the low effects observed after exposure to undigested PDNPLs were not observed in the digested ones. This indicated that the greater ability of digested PSNPLs to internalize was not accompanied by a greater hazard. This type of analysis should be performed with other MNPLs of varying sizes and chemical compositions.

1. Introduction

Due to the multiple advantages of plastic goods, including low cost, their use has experienced steady growth since the middle of the last century. Consequently, their presence in the environment, as waste, has not stopped growing and has become an important environmental concern (Lakshmi Kavya et al., 2020). Unfortunately, this plastic contamination has led to the introduction of micro/nanoplastics (MNPLs), resulting from the degradation of larger plastic materials, which are possibly more dangerous from a human health point of view (Bouwmeester et al., 2015; EFSA, 2016). Although the presence of MNPLs was initially associated with the marine environment, today, it is clear that MNPLs can be found in any type of environment (Mitrano et al., 2021). Consequently, humans are inescapably exposed, with inhalation and ingestion as the most frequent exposure routes. After exposure, MNPLs can translocate through physiological barriers, reach blood vessels, and internalize into different organs and tissues (Domenech et al., 2020; Fournier et al., 2020).

When ingestion is the exposure route of MNPLs, they are exposed to the digestion process taking part in the digestive tract, which may modify some of their physicochemical characteristics. The process starts in the mouth where saliva and amylase are present and follows in the stomach with the presence of strong acid gastric juices. Next, the gastric fluid is neutralized by the alkaline intestinal fluid, containing a multitude of enzymes required for food digestion. Accordingly, different *in vitro* approaches have been proposed to mimic this process (Kämpfer et al., 2020). Nevertheless, despite the usefulness of the *in vitro* digestion approaches, formal official validation of the static models is awaited.

☆ This paper has been recommended for acceptance by Michael Bank.

* Corresponding author. Group of Mutagenesis, Department of Genetics and Microbiology, Faculty of Biosciences, Universitat Autònoma de Barcelona, Campus of Bellaterra, 08193, Cerdanyola del Vallès, Barcelona, Spain.
E-mail address: ricard.marcos@uab.cat (R. Marcos).

https://doi.org/10.1016/j.envpol.2023.121656
Received 13 December 2022; Received in revised form 12 April 2023; Accepted 15 April 2023
Available online 17 April 2023

Thus, the consensus reached in the COST Action "Infogest" in 2014 has not yet generated validated guidelines (Colombo et al., 2021). Thus, the formation of a corona on the MNPL surface, induced by the influence of *in vitro* digestive treatment, has been reported to lead to changes in size, zeta potential, and the ability to adsorb compounds (Liu et al., 2020). When tire degradation particles were exposed *in vitro* to simulated gastric/intestinal fluids, the solubilization of heavy metal contents was greatly enhanced. It should be noted that metals, basically zinc, are used as catalysts during the vulcanization process of rubber, and consequently, they are components of the MNPLs resulting from tire degradation (Masset et al., 2021). Changes in the surface of the PETMPL samples were observed after *in vitro* intestinal digestion, as well as the presence of crystalline and organic deposits. These characteristics were considered relevant in the changes observed in their ability to attach to different bacterial phyla (Tamargo et al., 2022).

Once MNPLs cross protective barriers, they can reach the blood and interact with its components, including cells. Interestingly, it has been reported that MNPLs were able to differentially affect several white blood lineages in an *ex vivo* experiment using blood samples from different donors. While limited uptake was observed in lymphocytes, very high uptake was observed in monocytes and polymorphonuclear cells. In addition, significant increases in the levels of DNA damage were observed in monocytes and polymorphonuclear cells but not in lymphocytes (Ballesteros et al., 2020). These results agree with the data obtained *in vitro* using different hematopoietic cell lines, such as Raji-B (B-lymphocytes), TK6 (lymphoblasts), and THP-1 (monocytes), where exposure to nanopolystyrene produced differential effects on parameters such as cytotoxicity, cellular uptake, reactive oxygen species production, and genotoxicity (Rubio et al., 2020). In addition, it has been proven that after ingestion, in the digestive tract, MNPLs meet the intestinal mucosa and the intestinal epithelium, which constitute a barrier that helps to avoid the absorption of xenobiotics. Even considering this, several studies have shown that MNPLs can cross this biological barrier, reaching the circulatory system as well as more distant tissues and organs that include even the human placenta (Wright and Kelly, 2017; Banerjee and Shelver, 2021; Ragusa et al., 2021; Kumar et al., 2022).

In this context, our aim has been to identify if the application of *in vitro* digestion procedures can modulate some of the physicochemical characteristics of nanopolystyrene, used as a model of MNPLs. To this end, we used TEM, SEM, NTA, and Zetasizer devices to determine the size, morphology, hydrodynamic size, and surface charge. Furthermore, confocal Raman microscopy was applied to visualize and characterize proteins on the surface of MNPLs. Finally, changes in different biological characteristics, such as cell uptake, toxicity, intracellular ROS levels, and genotoxicity, were also determined.

2. Materials and methods

2.1. Nanopolystyrene selection, in vitro digestion, and dispersion preparation

Commercial polystyrene nanoplastics (PSNPLs, PP-008-10) with diameters of approximately 50–100 nm and their fluorescent yellow counterpart (fPSNPLs, FP-00552-2) with diameters of approximately 40–90 nm, obtained from Spherotech (Chicago, IL, USA), were used in this study.

According to the aim of this study, both PSNPLs and fPSNPLs were subjected to an *in vitro* digestion process following an adaptation of the method published by Mahler et al. (2009). This process mimics the particle/digestive fluid interactions that takes place in both the stomach and intestine compartments. Briefly, 0.40 g of PSNPLs (or 0.01 g of fPSNPLs) was dispersed in 10 mL of a sterile (140 mM NaCl, 5 mM KCl, pH = 2) solution, and the pH was adjusted to 2 with sterile 0.10 M HCl. A 0.50 mL sterile porcine pepsin solution (25 mg/mL diluted in 0.10 M HCl) was added and incubated for 1 h at 37 °C. Once the incubation was over, the pH of the samples was adjusted to 5.5–6 with sterile 0.10 M $NaHCO_3$. After that, 0.50 mL of sterile pancreatin-bile solution (1.40 mg/mL pancreatin and 8 mg/mL bile) was added to the sample, and the pH was adjusted to 6.9–7 using sterile 0.10 M $NaHCO_3$. The result of the indicated digestion process was weighed and adjusted to 15 g by using a sterile (140 mM NaCl, 5 mM KCl, pH = 6.7) solution. All the simulated digestive juices were prepared under sterile conditions. The digested polystyrene nanoplastics are hereafter referred to as dPSNPLs.

One milliliter of the mix containing all the components used in the digestion process (18750 μg/mL) was dispersed in 0.05% sterilized bovine serum albumin (BSA) and 30 μL of ethanol (100%) to reach a stock concentration of 3.125 μg/mL and then dispersed by ultrasonication in a cold-water bath. The digested fluorescent polystyrene nanoplastics (dfPSNPL), at a concentration of 725 μg/mL, were also dispersed by ultrasonication. All these steps followed the dispersion procedure generated in the EU project Nanogenotox (Nanogenotox, 2011). The dfPSNPLs were used only for the internalization and uptake assays, whereas dPSNPLs were used for the remaining assays.

2.2. Characterization of digested/undigested PSNPLs

2.2.1. Transmission electron microscopy (TEM)

The different particle dispersions (PSNPLs, dPSNPLs, fPSNPLs, and dfPSNPLs) were diluted in distilled water to obtain a 200 μg/mL concentration, mounted on carbon-coated TEM grids, and visualized with a JEOL JEM-1400 instrument (JEOL LTD, Tokyo, Japan). To determine their mean size and distribution, 100 randomly selected particles were measured by using ImageJ software.

2.2.2. Scanning electron microscopy (SEM)

The different NPL dispersions were diluted in distilled water to reach a concentration of 200 μg/mL, and a drop of each dispersion was placed over a silica grid and allowed to evaporate overnight. NPL characteristics were visualized with an SEM Zeiss Merlin device (Zeiss, Oberkochen, Germany) coupled with an X-Max 20 mm EDS system (Oxford Instruments, Oxford, UK). Once the signals were recorded, they were analyzed by using INCA Energy software.

2.2.3. Dynamic light scattering (DLS) and zeta potential

The hydrodynamic size was analyzed using a Zetasizer® Ultra from Malvern Panalytical. To proceed, PSNPLs, dPSNPLs, fPSNPLs, and dfPSNPLs at a concentration of 100 μg/mL were prepared in Milli-Q water, and the surface charge was determined by zeta potential values. The hydrodynamic size was determined by DLS. All the parameters for each sample were measured in triplicate.

2.2.4. Nanotracking analysis (NTA)

A NanoSight LM10 (NanoSight, Amesbury, United Kingdom) device equipped with a 532-nm laser was used for NTA measurements. NTA 3.0 software was used to capture and analyze the data. Samples were injected in the sample chamber, and a digital CCD camera detected the light scattered off the particles with a 20× microscope objective. The NTA software allowed the detection of each individual diffusion track and the determination of the hydrodynamic diameter of the particles. The particle concentration was set to 10^8–10^9 particles/mL by diluting the solution in Millipore water. Each sample was measured for 60 s at five different positions for three replicates. All measurements were performed at a temperature of 25 °C.

2.2.5. Confocal Raman microspectroscopy (CRM)

CRM was performed using an Alpha300 R microscope (WITec GmbH, Germany). PSNPLs, at a concentration of 312.5 μg/mL, were dried on glass slides, and Raman spectra were recorded pixelwise in the lateral plane using a laser power of ca 35 mW, an integration time of 0.15 s, and a step size of 250 nm. The images and single spectra were analyzed using Project FIVE PLUS software (WITec GmbH, Ulm, Germany). A watershed algorithm was applied to identify single particles and to determine

their amount of protein and coverage level. A total of 53 particles, such as single particles and their agglomerates, were analyzed.

2.3. Cells used and culture conditions

Three human cell types were selected for this study, namely, TK6 (lymphoblasts), THP-1 (monocytes), and Raji-B (B-lymphocytes). We selected lymphoblastic cells because once MNPLs cross the biological barriers, they reach the blood compartment, interacting with cells equivalent to those used in this study. This is the rationale for using the selected cells, which were purchased from Sigma Aldrich (MO, USA). The three different cell lines were cultured at 37 °C in a humidified atmosphere of 5% CO_2 and 95% air and maintained in 25 cm^2 culture flasks with RPMI (Biowest, France) supplemented with 10% FBS, 1% glutamine (Biowest, France), and 2.5 μg/mL Plasmocin™ (InvivoGen, CA, USA). The cell density range was kept from 5×10^5 cells/mL to 1×10^6 cells/mL (Rubio et al., 2020).

2.4. Cell internalization by flow cytometry

Flow cytometry (FC) was used to measure cell internalization. To proceed, cell suspensions seeded in 96 U-type well plates were treated for 24 h with different concentrations of fPSNPLs and dFPSNPLs. The exposed cells were analyzed using a Beckman Coulter CytoFlex S (Indianapolis, USA) device, and the obtained data were analyzed using CytExpert software. Three independent experiments using duplicates for each concentration were carried out.

2.5. fPSNPL and dfPSNPL intracellular localization by confocal microscopy

Laser confocal microscopy was used to confirm the internalization of the fPSNPLs and dfPSNPLs by the three cell lines, as previously reported (Cortés et al., 2022). Following the published protocol, fPSNPs and dfPSNPs were visualized inside cells. The obtained images were processed using ImageJ software. In addition, the images were also analyzed by using IMARIS 9.5 software for 3D/4D image analysis to better place PSNPLs inside the cell structure. Unexposed cells were used as a negative control for both experimental approaches.

2.6. Cell viability

Viability assays were performed as previously reported (Rubio et al., 2020). Samples from the three selected cell lines were exposed to PSNPLs/dPSNPLs at concentrations up to 200 μg/mL over 24 and 48 h. The treated cells were diluted 1:100 in ISOTON® and counted in a Beckman Coulter Counter Z2 (Indianapolis, USA). Three different experiments were performed, and in each experiment, three replicates were carried out. The average number of cells counted in each treatment was compared with the average number of untreated control cells. The results from the viability assay are useful to determine the range of noncytotoxic concentrations to be used in further experiments.

2.7. Reactive oxygen species (ROS) quantification

The production of intracellular reactive oxygen species (ROS) was determined using the dihydroethidium (DHE, Calbiochem, USA) assay and measured by FC. The three cell lines were exposed for 3 and 24 h to the selected concentrations of dPSNPLs. Cigarette smoke condensate (CSC, 100 μg/mL, Murty Pharmaceuticals, USA) was used as a positive control. Following a previously published protocol (Rubio et al., 2020), cells were analyzed by using a FACSCanto Flow Cytometer (BD Bioscience, USA) to evaluate a total of 10,000 events from living cells. For each condition, three independent experiments (with duplicate samples) were run.

2.8. Genotoxic and oxidative DNA damage induction

In a previous study carried out by our group, the genotoxic and oxidative DNA damage (ODD) induced by PSNPLs were determined (Rubio et al., 2020). The same methodology was used to evaluate the effects of dPSNPL exposure. The induced DNA damage was measured according to the percentage of DNA in the comet tails obtained using Komet 5.5 image analysis software (Kinetic Imaging Ltd., Liverpool, UK). Methyl methanesulfonate and potassium bromate were used as positive controls for general genotoxic damage and for ODD, respectively.

3. Results and discussion

3.1. Particle characterization

3.1.1. Morphology, dry state size distribution, and shape

PSNPLs, dPSNPLs, fPSNPLs, and dfPSNPLs were determined by TEM and SEM to visualize their size and morphology. The Martin diameter was measured by using TEM, and the size distribution was determined by measuring three times 100 images of each PSNPL type. The relative percentages of the different particle sizes are represented in Supplementary Fig. 1. Both TEM/SEM images show that all particles were spherically shaped, and the average sizes of the nondigested particles were approximately 66.07 nm for PSNPLs and 51.71 nm for fPSNPLs. These sizes agreed with the manufacturer's specifications. Once the particles were submitted to the *in vitro* digestion process, the obtained average TEM sizes were slightly modified to approximately 60.68 nm for dPSNPLs and 54.81 nm for dfPSNPLs. Although TEM and SEM images showed that the nondigested and the *in vitro* digested particles were similar in appearance and sizes, the images of the digested *in vitro* particles showed a relevant tendency to agglomerate, higher than in the nondigested particles, forming large groups of particles. This high agglomeration status was very evident from the SEM figures corresponding to the dfPSNPL condition. TEM/SEM analyses are not usually carried out in studies evaluating the effects of *in vitro* digestion (Liu et al., 2020); nevertheless, in a very recent study (Chen et al., 2022), no changes in size or shape were reported, confirming our findings as well as those obtained with different plastic materials such as polyethylene, polypropylene, polyvinyl chloride, polyethylene terephthalate, and polystyrene (Stock et al., 2020). These *in vitro* digestion effects would differ from those observed *in vivo* in the intestine of *Drosophila* larvae. When Drosophila larvae were exposed to three sizes of polystyrene MNPLs (50, 200, and 500 nm), differences were observed by TEM between sizes in the initial dispersion and into the intestine lumen. However, these differences were observed only for the highest sizes (200 and 500 nm) and not for 50 nm, which was the size used in our study (Alaraby et al., 2022).

3.1.2. Aqueous solution size distribution and zeta potential

The hydrodynamic size was determined by DLS for the four conditions. As observed in Supplementary Fig. 2, in general, the digested particles had a larger hydrodynamic size than the nondigested particles. In addition, the nondigested particles had a greater number of particles below 100 nm compared with the digested particles that showed more particles over 100 nm in size. This would agree with a higher ability of digested particles to agglomerate. This was also in accordance with the polydispersity index (PdI) values, where the nondigested particles were more dispersed than the digested ones. It should be remembered that values closer to 0 indicate that the sample is monodisperse. Changes in the hydrodynamic size after *in vitro* digestion have also been reported as a consequence of the presence of an induced corona on the surface of 100 nm polystyrene NPLs (Liu et al., 2020). The results obtained from the Z-potential measurements also agreed with those reported above, showing that the digested particles had a lower Z-potential than the nondigested particles. All these results indicate that the *in vitro* digested

particles presented a higher tendency to agglomerate than the non-digested particles.

3.1.3. Nanotracking analysis (NTA)

Additionally, the number size distribution was determined by means of NTA (Fig. 1). NTA is a more reliable tool for the evaluation of polydisperse samples, as it is based on single particle tracking. Nanotracking analysis revealed similar mode values of 75 nm for digested and undigested PS particles. This value was higher than the diameter obtained by TEM, as NTA measures the hydrodynamic radius, which represents not only the hard core of PS particles but also solvent molecules and ions that surround them. On the other hand, DLS measurements showed a higher particle diameter. DLS delivers an intensity-weighted distribution of particles that is highly sensitive to large particles.

Similar to the TEM and DLS results, NTA showed a higher polydispersity of digested PS particles with the presence of various agglomerated populations at 140 nm and approximately 200 nm, which were roughly double and triple the size of the initial particle size. PSNPLs showed only a small additional accumulation at 140 nm (Fig. 1).

3.1.4. Visualization and characterization of proteins on the surface of PS particles

The Raman spectrum of PS particles has characteristic modes, such as ring breathing at 1001 cm^{-1}, CH in-plane deformation at 1031 cm^{-1}, CH_2 deformation at 1450 cm^{-1}, ring skeletal stretching at 1602 cm^{-1}, symmetric stretching at 2852 cm^{-1} and asymmetric CH_2 aliphatic stretching modes at 2904 cm^{-1}, as well as CH ring stretching at 3054 cm^{-1} (Hong et al., 1991; Mazilu et al., 2010; Nava et al., 2021). The ring breathing mode of PS has been used for visualization of dPSNPLs (Fig. 2a). Fig. 2b shows the average spectra of PSNPLs and dPSNPLs that were extracted from regions identified as particles in CRM images. This ensured that only proteins located on the particle surface would be analyzed. Compared to undigested particles, the spectrum of dPSNPLs revealed additional bands related to proteins. The intensity of bands related to CH_2 deformation and stretching region of proteins at 1450 cm^{-1}, 2852 cm^{-1}, and 2904 cm^{-1} were increased. Furthermore, additional bands corresponding to the symmetrical CH_3 mode of proteins at 2936 cm^{-1} and to the amide I region of proteins at approximately 1660 cm^{-1} were recorded (Carey, 2006; Rygula et al., 2013). The overlapping map image of the amide I distribution with that of digested PS particles shows an association of proteins on the particle surface (Fig. 2a).

The region of the amide I band was thoroughly analyzed to obtain information about the secondary protein structure on the particle surface, as well as PS polymer degradation due to the digestion process. To this aim, the spectrum of undigested PS was subtracted from that of dPSNPLs, leaving only the protein signal associated with the particle. Fitting of the amide I band revealed the occurrence of random coils, alpha helices, and beta sheets at 1640 cm^{-1}, 1660 cm^{-1}, and 1680 cm^{-1}, respectively (Maiti et al., 2004) (Fig. 2c). The large amount of beta sheets might have originated from pepsin, which has 44% beta sheets and only 14% alpha helices (Sielecki et al., 1990; Berman et al., 2000). Amylase can also contribute to beta sheet formation with 23% of the beta fraction (Ragunath et al., 2008). In contrast, BSA has a mainly alpha helix structure (Lin and Koenig, 1976). The fitting showed an additional band at 1629 cm^{-1} that was associated with monomeric PS (Sears et al., 1981; Noda and Sala, 2000). It might be assumed that a small number of monomers were generated due to the degradation of the polymer caused by digestion.

Furthermore, CRM images of digested PS particles were analyzed at the single particle level by using a watershed algorithm. The degree of coverage with protein and the semiquantification of the protein amount on the particle surface across a particle population are summarized in Fig. 3.

As observed, most of the particles showed only a small degree of coverage with proteins on their surface. On average, 7.7% of the surface area of particles was covered by proteins. However, some particles showed coverage of 20%–45%, which indicated strong differences between the particles (Fig. 3a). Approximately 30% of the particles showed no protein association. Fig. 3b shows a histogram of semiquantification of protein on digested particles across the particle population. The semiquantification was based on the calculated ratio of the integral intensity of the amide I band to that of the PS mode at 1001 cm^{-1} for each particle. Most of the particles showed only small amounts of associated protein. Similar to the particle coverage distributions, there were large differences between the particles, which indicated a heterogeneous distribution of protein amount on the particle surface (Fig. 3). The presence of proteins on the surface of digested particles has also been found in other studies, although the content was modulated by size, being higher in 100 nm PS MNPLs than in 5 μm PS MNPLs (Liu et al., 2020).

3.2. Cell internalization

The cellular uptake of both fPSNPLs and dfPSNPLs was determined by flow cytometry. The study involved three cell lines, an exposure period of 24 h, and five concentrations (1, 5, 10, 25, and 50 μg/mL). Fig. 4 shows that for the three cell lines, the observed fluorescence values were higher after dfPSNPL exposure than with the undigested counterpart. Such an effect was observed at all the tested concentrations and in the three cell lines. Interestingly, at the highest concentration (50 μg/mL) of dfPSNPLs, almost 100% of the three cell lines showed fluorescent signals. Regarding the uptake of fPSNPLs, marked differences were observed between cell lines, with Raji-B cells showing higher uptake, followed by THP1 cells, with TK-6 showing lower uptake. When

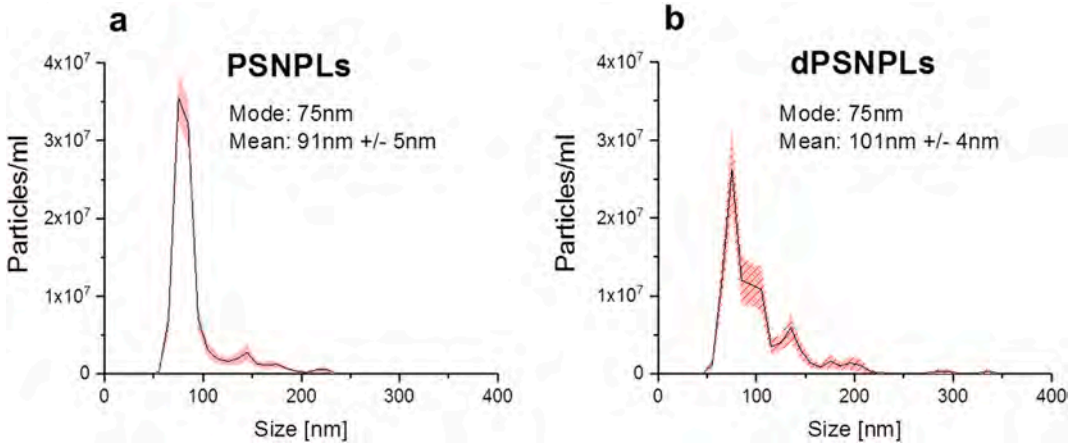

Fig. 1. Nanotracking analysis of undigested (a) and digested (b) PS particles.

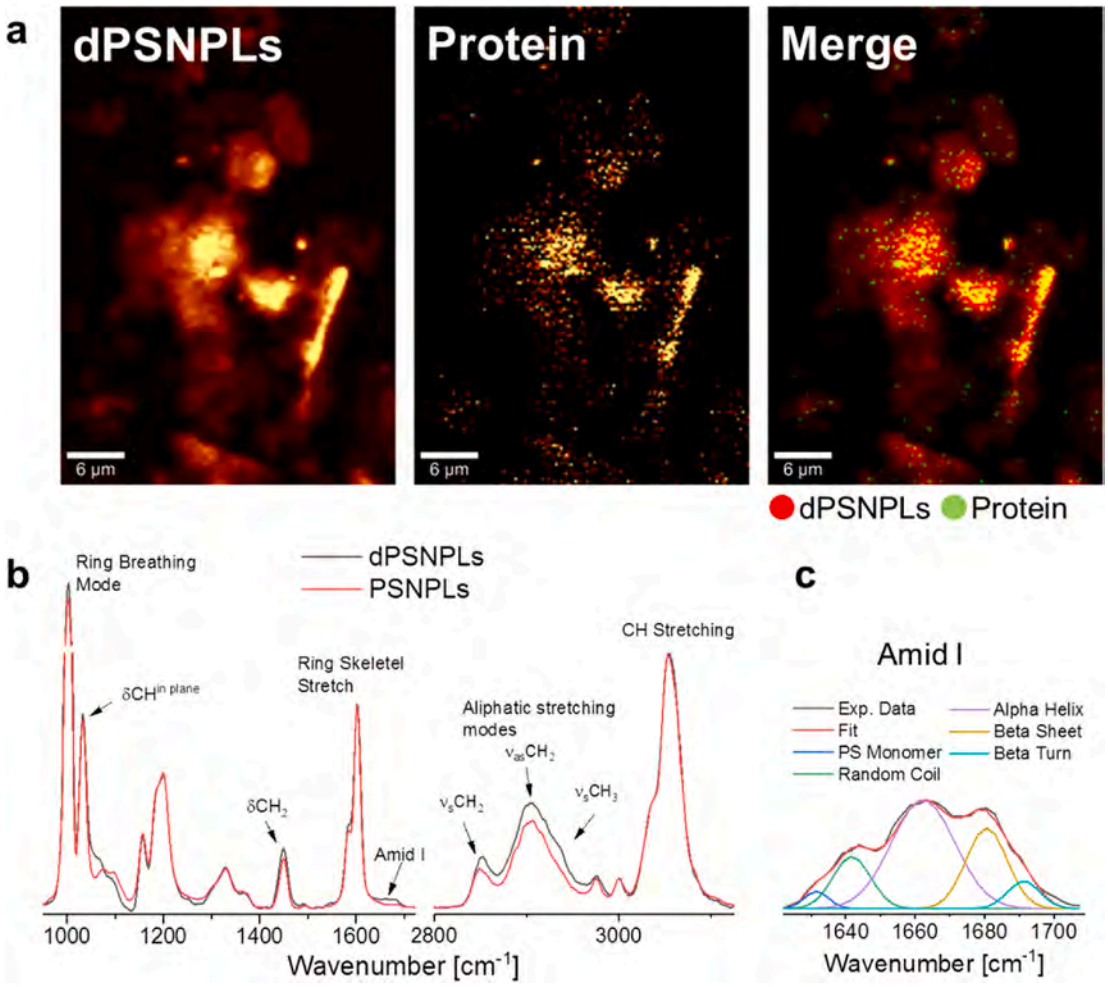

Fig. 2. CRM analysis of PSNPLs and dPSNPLs: (a) the color-coded images of dPSNPLs (left), proteins (middle) and their overlapping (right); (b) Raman spectra of digested and undigested particles extracted from region of interest; (c) fitting analysis of amid I band represented a secondary structure of proteins on the surface of digested particles. (For interpretation of the references to color in this figure legend, the reader is referred to the Web version of this article.)

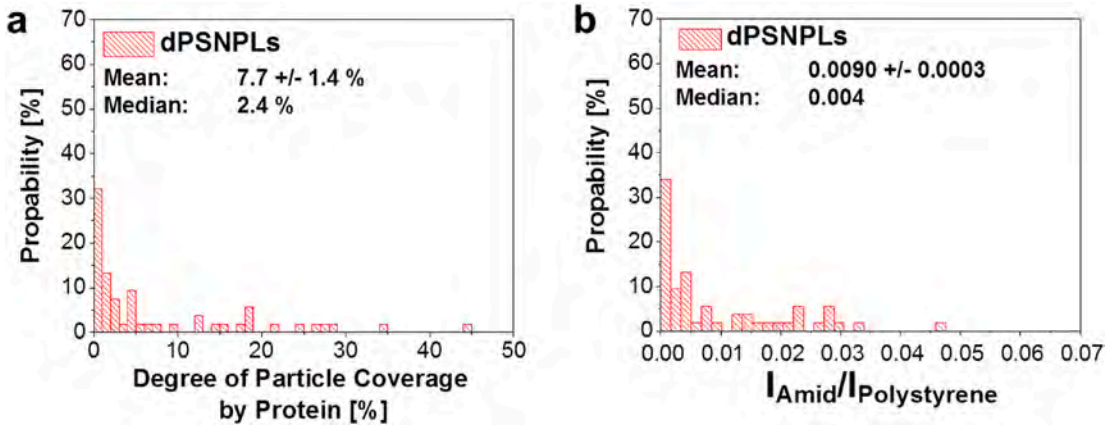

Fig. 3. Histograms of degree of protein coverage (a) and protein amount (b) on the surface of single dPSNPLs across a particle population.

the uptake reached after exposure to the highest concentration (50 µg/mL) was compared, in Raji-B cells, almost 80% of the cells showed fluorescence, whereas the observed values for THP1 and TK6 cells were 35% and 20%, respectively. These results agreed with previously reported data for the same three cell lines used (Rubio et al., 2020). Interestingly, this different uptake between human hematopoietic cell lines was also detected in *vivo* studies. Thus, when different subsets of white peripheral blood cells (namely, lymphocytes, monocytes, and polymorphonuclear cells) were sorted from whole blood samples of different donors, sharp differences in cell uptake between cell types were observed. Thus, very limited uptake was observed in lymphocytes, very high uptake in monocytes, and intermediate uptake values for polymorphonuclear cells (Ballesteros et al., 2020). This indicates that uptake is modulated not only by the physicochemical characteristics of the

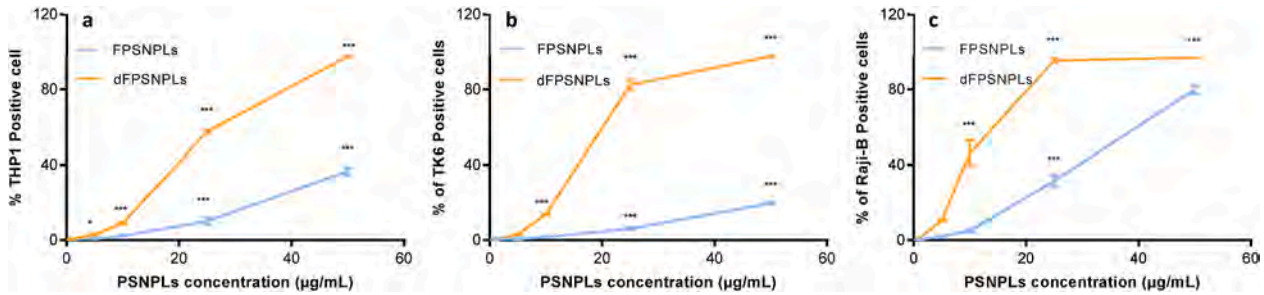

Fig. 4. Cellular internalization of fPSNPLs and dfPSNPLs by THP-1 cells (a), TK6 cells (b), and Raji-B cells (c), after exposures lasting for 24 h. The graph represents the percentage of fluorescent-positive cells over the total cell population. Data are analyzed by the one-way ANOVA test with a Dunnett's post-test. Statistical significance indicated in the graph correspond to $^{*}P < 0.05$, $^{**}P < 0.01$, $^{***}P < 0.001$.

MNPLs but also by the cell type used.

Unfortunately, no studies have evaluated differences in cell uptake between digested and undigested MNPLs. The study evaluating cell uptake and translocation of digested MNPLs in an *in vitro* coculture model of the intestinal barrier did not compare digested *vs.* undigested MNPLs (DeLoid et al., 2021).

3.3. Intracellular presence of fPSNPLs and dfPSNPLs

To determine the cellular location of both fPSNPLs and dfPSNPLs in the three cell types, confocal microscopy was used at a concentration of 100 μg/mL and exposures lasting for 24 h. As observed in Fig. 5, both types of particles were found inside the three cell lines, in agreement with the uptake indicated in the previous section. PSNPLs were not localized in specific regions, and no relevant differences were observed between digested and nondigested particles. Thus, particles were observed attached to the membrane of the cells, spread into the cytoplasm, or accumulated in the perinuclear areas. Interestingly, particles were also internalized into the nucleus. These results agreed with those previously reported in the same three hematopoietic cell lines (Rubio et al., 2020). The localization of PSNPLs into cells has also been reported in undifferentiated human intestinal Caco-2 cells (Cortés et al., 2020), as well as in cocultures of differentiated Caco-2 cells forming an *in vitro* intestinal barrier (Domenech et al., 2020).

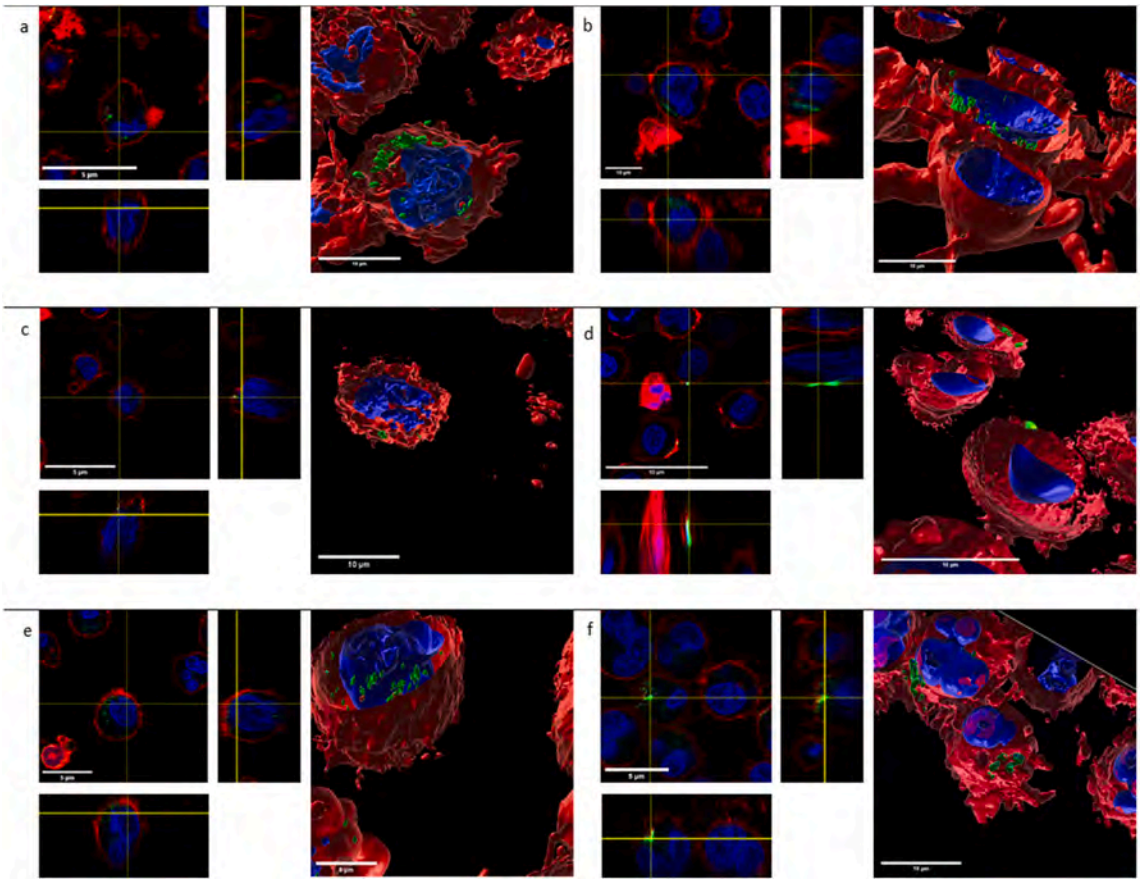

Fig. 5. Selection of representative three-dimensional images of THP1, TK6, and Raji-B cells exposed to 100 μg/mL of dfPSNPLs (left) and fPSNPLs (right) for 24 h. (a) and (b) represent THP1 cells; (c) and (d) represent TK6 cells; and (e) and (f) represent Raji-B cells. dfPSNPL and fPSNPL particles are shown in green, nuclei in blue, and cell membranes are red. ImageJ was used to process the figures, and the Imaris 9.5 software was use for obtaining 3D/4D images. (For interpretation of the references to color in this figure legend, the reader is referred to the Web version of this article.)

3.4. Cytotoxicity assessment

To determine the potential cytotoxic concentrations of PSNPLs and dPSNPLs, a viability assay was carried out on TK6, THP1, and Raji-B cells. The range of tested concentrations was from 0 μg/mL (negative control) to 200 μg/mL, and the exposures lasted for 24 and 48 h. The obtained results are indicated in Supplementary Fig. 3. The significant effects, when they existed, were always observed at the highest concentrations tested (150/200 μg/mL), which were very high concentrations and, consequently, unrealistic exposures. Consequently, PSNPLs could be considered nontoxic compounds, independent of whether they are digested. Furthermore, the exposure time modulated the effects, which were always higher after 48 h of exposure. Finally, the effects of digestion were only remarkable on the TK6 cells and at the longer exposure time (48 h). According to the toxicity data and aiming to work with noncytotoxic doses, concentrations ≤50 μg/mL were chosen for the rest of the assays. The potential toxicity of MNPLs has been recently reviewed (Schröter and Ventura, 2022), and the lack of important cytotoxicity is usually reported, as in human lung and intestinal cells (Zhang et al., 2022), where three different polystyrene nanoplastic sizes were evaluated.

3.5. Production of intracellular ROS

To determine the intracellular levels of ROS induced by dPSNPL exposure, a DHE assay was used. DHE (dihydroethidium) easily crosses cell membranes reacting with intracellular superoxide anions. This reaction produces a red fluorescent compound (2-hydroxyethidium), which can intercalate into DNA. Fig. 6 represents the intracellular ROS production measured with the DHE assay by using FC. The three cell lines were exposed to different concentrations from 0 to 50 μg/mL with exposures lasting for 3 and 24 h. The figure shows an increased production of ROS after exposure lasting for 3 h, but only at the highest concentration (50 μg/mL) and in TK6 and Raji-B cells. These effects were increased in exposures lasting for 24 h, but only in the TK6 cell line, which seemed to be especially sensitive to PSNPL effects. These effects were not observed when cells were exposed to the digested PSNPLs. The induction of oxidative stress by nanoparticle exposure has been accepted as a regular mechanism of action (Li et al., 2022). This assumption has been proposed in the case of MNPLs, but the obtained results are usually weak and contradictory (Yong et al., 2020). Positive induction, according to the cell type, was demonstrated previously (Rubio et al., 2020), and the ability to induce oxidative stress has also been associated with surface functionalization (He et al., 2020). Unfortunately, no studies have compared the ability of *in vitro* digested MNPLs to induce oxidative stress, which highlights the interest in the results reported in this study.

3.6. Genotoxic and oxidative DNA damage

The comet assay (with and without FPG) was carried out to measure DNA damage induced by the different exposures of PSNPLs. The three cell lines were exposed to different concentrations of PSNPLs and dPSNPLs at two different time points, 3 and 24 h. The obtained results are indicated in Figs. 7 and 8 for exposures lasting for 3 and 24 h, respectively. Fig. 7 shows the results at exposures lasting for 3 h, and as observed, no genotoxic or oxidative damage was observed in any of the three cell lines. This means that under these exposure conditions, no differences were observed between PSNPLs and dPSNPLs.

The results obtained in exposures lasting for 24 h are presented in

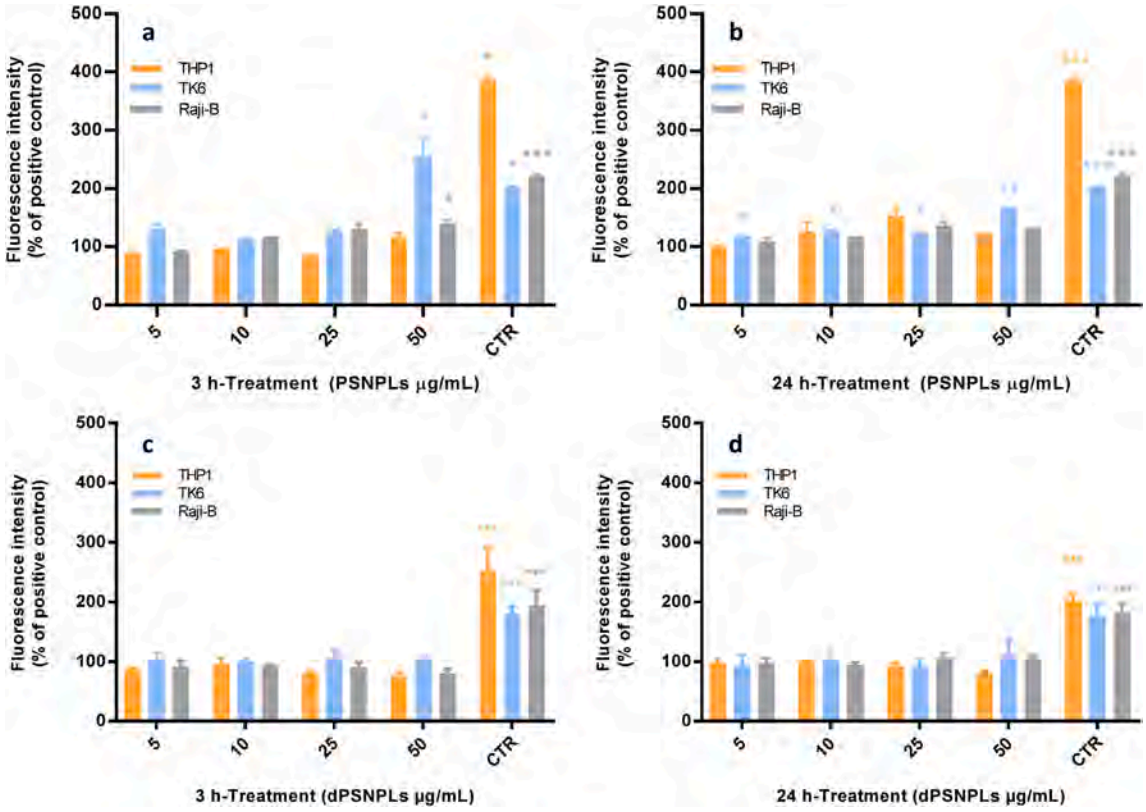

Fig. 6. Intracellular ROS production analysis in THP1, TK6 and Raji-B cells exposed to both PSNPLs and dPSNPLs. Exposures lasted for 3 h (**a** and **c**) and 24 h (**b** and **d**). Exposure to 100 μg/mL CSC was used as positive control (CRT). ROS production was extrapolated from the average of the mean fluorescence intensity from three independent experiments with duplicated samples (10,000 events taken from the living cell population for each sample). Data are represented as the percentage of fluorescence intensity compared to the negative control. One-way ANOVA with Dunnett's post-test was used for the statistical analysis. Statistical significance was indicated in the graph as *P < 0.05, **P < 0.01, and ***P < 0.001.

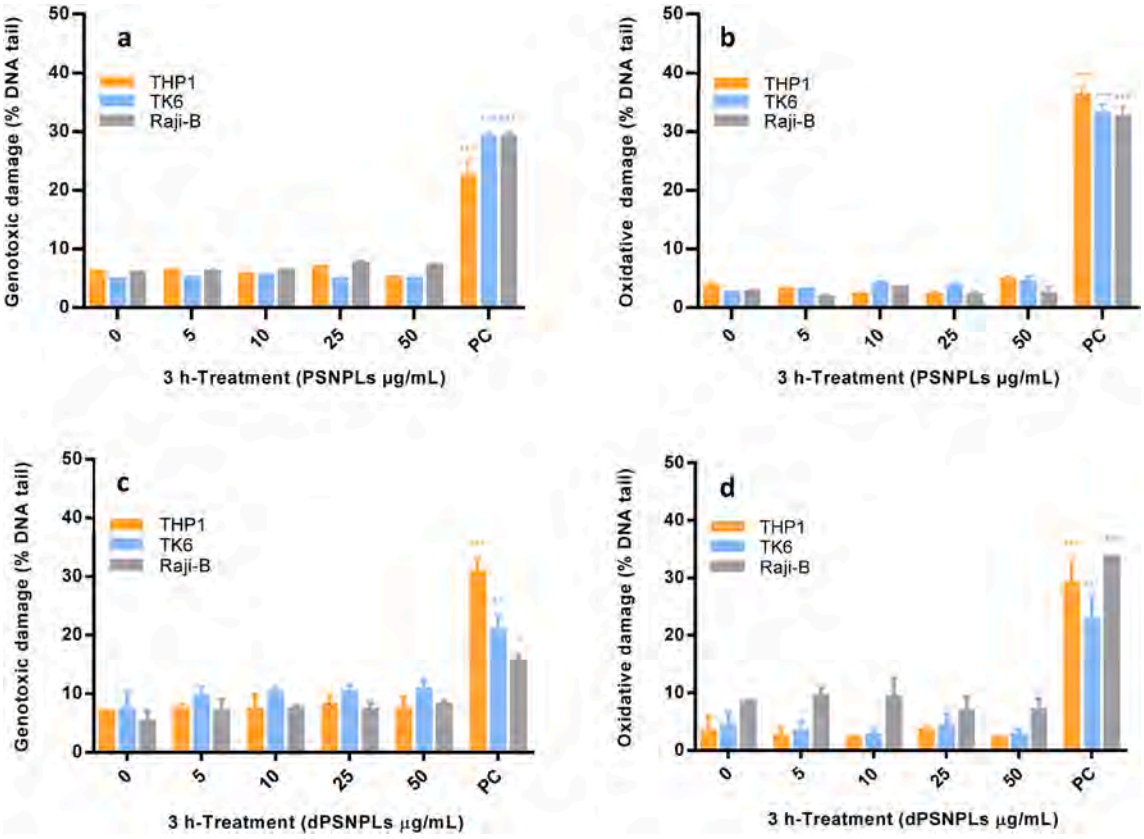

Fig. 7. Genotoxic and oxidative damage detected by the comet assay after 3 h of exposure to PSNPLs (a, b) and to dPSNPLs (c, d). Oxidative DNA damage (ODD) was detected using the FPG enzyme. The concentration of 200 µM of methyl methanesulfonate (MMS) was used as a positive control (PC) for genotoxic damage induction while 5 mM of potassium bromate ($KBrO_3$) was used as positive control for ODD. Experiments were performed with duplicates and 100 randomly selected cells were analyzed by the Komet 5.5 software. Data are represented as mean ± SEM and analyzed by the one-way ANOVA test with a Dunnett post-test. Statistical significance was indicated in the graph as follow, $*P < 0.05$, $**P < 0.01$, $***P < 0.001$.

Fig. 8. When the genotoxic damage was analyzed (a and c), slight effects were observed in both exposures, PSNPLs and dPSNPLs, although with differences between cell lines. Thus, PSNPL exposure induced effects only in Raji-B cells at the highest concentrations (25 and 50 µg/mL). On the other hand, dPSNPLs induced statistically significant effects only in THP1 cells, although a tendency to show high DNA damage was also observed in Raji-B cells.

When the ability to induce oxidative damage in the DNA bases was determined, differences between exposures were observed. In that case, the induced effects observed, mainly in the TK6 cells after exposure to PSNPLs, were not observed when the effects of dPSNPLs were evaluated. Interestingly, these results matched well with the results obtained in the experiments evaluating the induction of intracellular ROS levels. Globally, some genotoxic effects are observed to be associated with exposure, although such effects can be considered mild if they truly exist. Thus, when the observed effects were low and without a concentration-dependent relationship, simple stochastic effects could be responsible for the observed "significant" effects.

The link between ROS induction and genotoxicity is well known (Quezada-Maldonado et al., 2021), which supports our findings. Nevertheless, the potential genotoxicity of MNPLs is a topic that has generated conflicting consensus, since contradictory results have been reported (Xu et al., 2022). Different reasons can be associated with the contradictory genotoxicity data. First, under the MNPL umbrella, there is great variability in size that can affect the genotoxicity outcome. Alternatively, the cell line used is another potential source of variability since MNPL uptake is cell dependent. Finally, there is the genotoxic potential (if it exists) of MNPLs, since it is weak, and a large variability is expected based only on a probabilistic point of view.

4. Conclusions

One of the main exposure routes for MNPLs is ingestion. Their long journey through the different compartments of the intestinal tract can modify some of their properties, such as size and surface, before reaching the intestinal barrier. These changes would be a consequence of the accompanying digestion processes. Consequently, modifications in their uptake ability and their distribution through the entire body can occur. We explored whether the *in vitro* digestion of polystyrene nanoplastics (PSNPLs) of approximately 50 nm can modify some of their properties. First, independent of the method used (TEM, DLS, or NTA), no relevant differences in size were found between undigested and digested PDNPLs. Nevertheless, a higher tendency of digested PSNPLs to agglomerate was observed, and CRM indicated the differential presence of proteins on the surface of digested particles. Interestingly, great differences in cell uptake were observed between nondigested and digested cells, with the latter showing greater uptake in the three tested cell lines. Despite these differences in cell uptake, no significant differences in toxicity were observed except for high and assumed unrealistic exposures. It is worth noting the different uptake capabilities observed between cell lines. Consequently, in addition to the physicochemical characteristics (including digested *vs.* undigested PSNPLs), the cell type used was a very relevant factor modulating cell uptake. When oxidative stress and genotoxicity induction were determined, the low effects observed after exposure to undigested PDNPLs were not observed in the digested ones. This was also observed when the different cell types were considered. This would indicate that the greater ability of digested PSNPLs to internalize was not accompanied by a greater hazard if not the opposite.

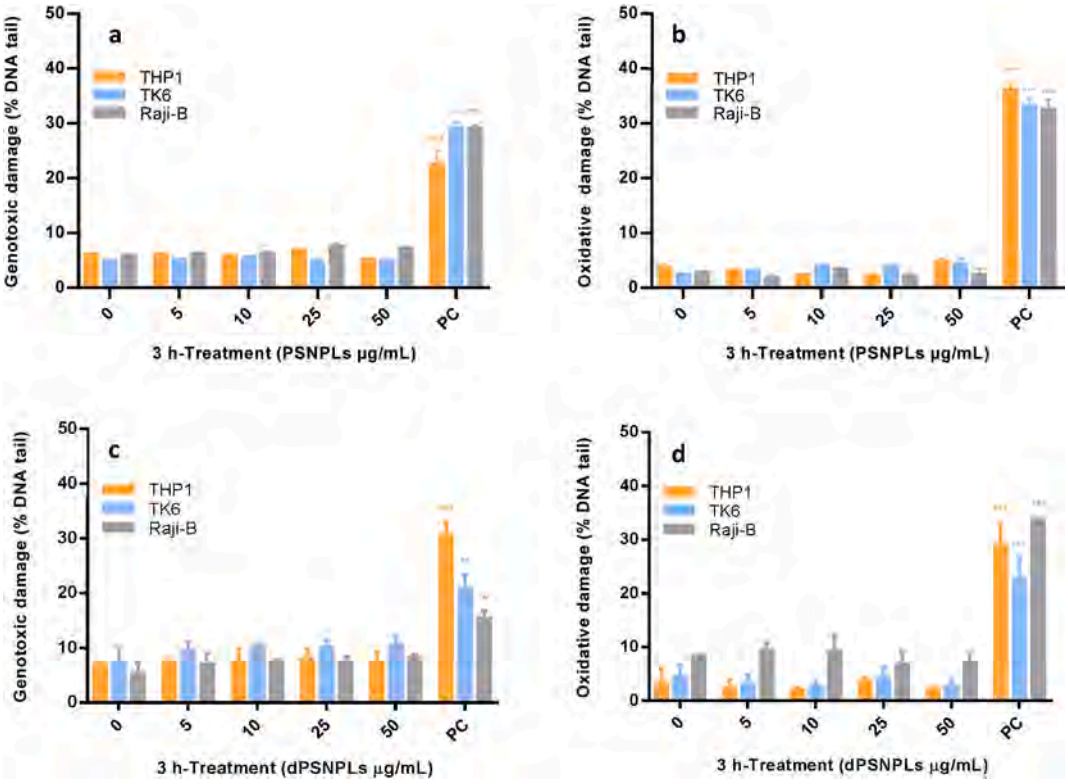

Fig. 8. Genotoxic and oxidative DNA damage detected by the comet assay after 24 h of PSNPLs (a, b) and dPSNPLs (c, d) exposures. The oxidative DNA damage (ODD) was detected using the FPG enzyme. The concentration of 200 µM of methyl methanesulfonate (MMS) was used as a positive control (PC) for genotoxic damage induction while 5 mM of potassium bromate ($KBrO_3$) was used as positive control for ODD. Experiments were performed with duplicates and 100 randomly selected cells were analyzed by the Komet 5.5 software. Data are represented as mean ± SEM and analyzed by the one-way ANOVA test with a Dunnett post-test. Statistical significance was indicated in the graph as follow, $^{*}P < 0.05$, $^{**}P < 0.01$ $^{***}P < 0.001$.

Author contribution statement

RM and AH planned the experiments. LV, AV, SP, AGR, and LR carried out the experimental part. LV, and AV analyzed the data, carried out the statistical analysis, and prepared tables/figures. TV and IEL were involved in the part containing NTA and CRM information. LV, RM, and AH wrote the final manuscript.

Declaration of competing interest

The authors declare that they have no known competing financial interests or personal relationships that could have appeared to influence the work reported in this paper.

Data availability

Data will be made available on request.

Acknowledgments

L. Vela was supported by PhD fellowships from the Fundación Carolina. A. Villacorta was supported by PhD fellowships from the National Agency for Research and Development (ANID), CONICYT PFCHA/DOCTORADO BECAS CHILE/2020–72210237. A. García-Rodríguez received funding from the postdoctoral fellowships program Beatriu de Pinós, funded by the Secretary of Universities and Research [Government of Catalonia] and by the Horizon 2020program of research and innovation of the European Union under the Marie Sktodowsdka-Curie grant agreement No 801370. L. Rubio was supported by a contract Juan de la Cierva [IJC 2020–2686I/AEI/10.13039/501100011033]. A. Hernández was granted an ICREA ACADEMIA award.

This project has received funding from the European Union's Horizon 2020 Research and Innovation Programme under Grant Agreement No. 965196. This work was also partially supported by the Spanish Ministry of Science and Innovation [PID 2020-116789, RB-C43] and by the Generalitat de Catalunya (2021-SGR-00731).

Appendix A. Supplementary data

Supplementary data to this article can be found online at https://doi.org/10.1016/j.envpol.2023.121656.

References

Alaraby, M., Abass, D., Domenech, J., Hernández, A., Marcos, R., 2022. Hazard assessment of ingested polystyrene nanoplastics in *Drosophila* larvae. Environ. Sci. Nano 9, 1845–1857. https://doi.org/10.1039/d1en01199e.

Ballesteros, S., Domenech, J., Barguilla, I., Cortés, C., Marcos, R., Hernández, A., 2020. Genotoxic and immunomodulatory effects in human white blood cells after *ex vivo* exposure to polystyrene nanoplastics. Environ. Sci.: Nano 7, 3431–3446. https://doi.org/10.1039/d0en00748j.

Banerjee, A., Shelver, W.L., 2021. Micro- and nanoplastic induced cellular toxicity in mammals: a review. Sci. Total Environ. 755 (Pt 2), 142518 https://doi.org/10.1016/j.scitotenv.2020.142518.

Berman, H.M., Westbrook, J., Feng, Z., Gilliland, G., Bhat, T.N., Weissig, H., Shindyalov, I.N., Bourne, P.E., 2000. The protein data bank. Nucleic Acids Res. 28, 235–242. https://doi.org/10.1093/nar/28.1.235.

Bouwmeester, H., Hollman, P.C., Peters, R.J., 2015. Potential health impact of environmentally released micro- and nanoplastics in the human food production chain: experiences from Nanotoxicology. Environ. Sci. Technol. 49 (15), 8932–8947. https://doi.org/10.1021/acs.est.5b01090.

Carey, P.R., 2006. Raman crystallography and other biochemical applications of Raman microscopy. Annu. Rev. Phys. Chem. 57, 527–554. https://doi.org/10.1146/annurev.physchem.57.032905.104521.

Chen, H., Chen, H., Nan, S., Liu, H., Chen, L., Yu, L., 2022. Investigation of microplastics in digestion system: effect on surface microstructures and probiotics. Bull. Environ. Contam. Toxicol. https://doi.org/10.1007/s00128-022-03571-x. Online ahead of print.

Colombo, R., Ferron, L., Frosi, Papetti A., 2021. Advances in static *in vitro* digestion models after the COST action Infogest consensus protocol. Food Funct. 12 (17), 7619–7636. https://doi.org/10.1039/d1fo01089a.

Cortés, C., Domenech, J., Salazar, M., Pastor, S., Marcos, R., Hernández, A., 2020. Nanoplastics as potential environmental health factors. Effects of polystyrene nanoparticles on the human intestinal epithelial Caco-2 cells. Environ. Sci.: Nano 7, 272–285. https://doi.org/10.1039/c9en00523d.

DeLoid, G.M., Cao, X., Bitounis, D., Singh, D., Llopis, P.M., Buckley, B., Demokritou, P., 2021. Toxicity, uptake, and nuclear translocation of ingested micro-nanoplastics in an *in vitro* model of the small intestinal epithelium. Food Chem. Toxicol. 158, 112609 https://doi.org/10.1016/j.fct.2021.112609.

Domenech, J., Hernández, A., Rubio, L., Marcos, R., Cortés, C., 2020. Interactions of polystyrene with *in vitro* models of the human intestinal barrier. Arch. Toxicol. 94 (9), 2997–3012. https://doi.org/10.1007/s00204-020-02805-3.

EFSA, 2016. Presence of microplastics and nanoplastics in food, with particular focus on seafood. EFSA J. 14 (6), 1–30. https://doi.org/10.2903/j.efsa.2016.4501.

Fournier, S.B., D'Errico, J.N., Adler, D.S., Kollontzi, S., Goedken, M.J., Fabris, L., Yurkow, E.J., Stapleton, P.A., 2020. Nanopolystyrene translocation and fetal deposition after acute lung exposure during late-stage pregnancy. Part. Fibre Toxicol. 17 (1), 55. https://doi.org/10.1186/s12989-020-00385-9.

He, Y., Li, J., Chen, J., Miao, X., Li, G., He, Q., Xu, H., Li, H., Wei, Y., 2020. Cytotoxic effects of polystyrene nanoplastics with different surface functionalization on human HepG2 cells. Sci. Total Environ. 723, 138180 https://doi.org/10.1016/j.scitotenv.2020.138180.

Hong, P.P., Boerio, F.J., Clarson, S.J., Smith, S.D., 1991. An investigation of the interdiffusion of polystyrene and deuterated polystyrene using surface-enhanced Raman-Scattering. Macromolecules 24, 4770–4776. https://doi.org/10.1021/ma00017a007.

Kämpfer, A.A.M., Busch, M., Schins, R.P.F., 2020. Advanced *in vitro* testing strategies and models of the intestine for nanosafety research. Chem. Res. Toxicol. 33 (5), 1163–1178. https://doi.org/10.1021/acs.chemrestox.0c00079.

Kumar, R., Manna, C., Padha, S., Verma, A., Sharma, P., Dhar, A., Ghosh, A., Bhattacharya, P., 2022. Micro(nano)plastics pollution and human health: how plastics can induce carcinogenesis to humans? Chemosphere 298, 134267. https://doi.org/10.1016/j.chemosphere.2022.134267.

Lakshmi Kavya, A.N.V., Sundarrajan, S., Ramakrishna, S., 2020. Identification and characterization of micro-plastics in the marine environment: a mini review. Mar. Pollut. Bull. 160, 111704 https://doi.org/10.1016/j.marpolbul.2020.111704.

Li, B., Zhang, T., Tang, M., 2022. Toxicity mechanism of nanomaterials: focus on endoplasmic reticulum stress. Sci. Total Environ. 834, 155417 https://doi.org/10.1016/j.scitotenv.2022.155417.

Lin, V.J., Koenig, J.L., 1976. Raman studies of bovine serum albumin. Biopolymers 15, 203–218. https://doi.org/10.1002/bip.1976.360150114.

Liu, S., Wu, X., Gu, W., Yu, J., Wu, B., 2020. Influence of the digestive process on intestinal toxicity of polystyrene microplastics as determined by *in vitro* Caco-2 models. Chemosphere 256, 127204. https://doi.org/10.1016/j.chemosphere.2020.127204.

Mahler, G.J., Shuler, M.L., Glahn, R.P., 2009. Characterization of Caco-2 and HT29-MTX cocultures in an *in vitro* digestion/cell culture model used to predict iron bioavailability. J. Nutr. Biochem. 20 (7), 494–502. https://doi.org/10.1016/j.jnutbio.2008.05.006.

Maiti, N.C., Apetri, M.M., Zagorski, M.G., Carey, P.R., Anderson, V.E., 2004. Raman spectroscopic characterization of secondary structure in natively unfolded proteins: alpha-synuclein. J. Am. Chem. Soc. 126, 2399–2408. https://doi.org/10.1021/ja0356176.

Masset, T., Ferrari, B.J.D., Oldham, D., Dudefoi, W., Minghetti, M., Schirmer, K., Bergmann, A., Vermeirssen, E., Breider, F., 2021. *Vitro* digestion of tire particles in a fish model (*Oncorhynchus mykiss*): solubilization kinetics of heavy metals and effects of food coingestion. Environ. Sci. Technol. 55 (23), 15788–15796. https://doi.org/10.1021/acs.est.1c04385.

Mazilu, M., De Luca, A.C., Riches, A., Herrington, C.S., Dholakia, K., 2010. Optimal algorithm for fluorescence suppression of modulated Raman spectroscopy. Opt Express 18, 11382–11395. https://doi.org/10.1364/OE.18.011382.

Mitrano, D.M., Wick, P., Nowack, B., 2011. Placing nanoplastics in the context of global plastic pollution, 2021 Nat. Nanotechnol. 16 (5), 491–500. https://doi.org/10.1038/s41565-021-00888-2. Nanogenotox. http://www.nanogenotox.eu/files/PDF/Deliverables/nanogenotox%20.

Nanogenotox. http://www.nanogenotox.eu/files/PDF/Deliverables/nanogenotox%20deliverable%203_wp4_%20dispersion%20protocol.pdf.

Nava, V., Frezzotti, M.L., Leoni, B., 2021. Raman spectroscopy for the analysis of microplastics in aquatic systems. Appl. Spectrosc. 75, 1341–1357. https://doi.org/10.1364/AS.75.001341.

Noda, L.K., Sala, O., 2000. A resonance Raman investigation on the interaction of styrene and 4-methyl styrene oligomers on sulphated titanium oxide. Spectrochim. Acta A. Mol. Biomol. Spectrosc. 56A, 145–155. https://doi.org/10.1016/S1386-1425(99)00128-6.

Quezada-Maldonado, E.M., Sánchez-Pérez, Y., Yi, Chirino, García-Cuellar, C.M., 2021. Airborne particulate matter induces oxidative damage, DNA adduct formation and alterations in DNA repair pathways. Environ. Pollut. 287, 117313 https://doi.org/10.1016/j.envpol.2021.117313.

Ragunath, C., Manuel, S.G., Venkataraman, V., Sait, H.B., Kasinathan, C., Ramasubbu, N., 2008. Probing the role of aromatic residues at the secondary saccharide-binding sites of human salivary alpha-amylase in substrate hydrolysis and bacterial binding. J. Mol. Biol. 384, 1232–1248. https://doi.org/10.1016/j.jmb.2008.09.089.

Ragusa, A., Svelato, A., Santacroce, C., Catalano, P., Notarstefano, V., Carnevali, O., Papa, F., Ciro, M., Rongioletti, A., Baiocco, F., Draghi, S., Amore, E.D., Rinaldo, D., Matta, M., Giorgini, E., 2021. Plasticenta : first evidence of microplastics in human placenta. Environ. Int. 146, 106274 https://doi.org/10.1016/j.envint.2020.106274.

Rygula, A., Majzner, K., Marzec, K.M., Kaczor, A., Pilarczyk, M., Baranska, M., 2013. Raman spectroscopy of proteins: a review. J. Raman Spectrosc. 44, 1061–1076. https://doi.org/10.1002/jrs.4335.

Rubio, L., Barguilla, I., Domenech, J., Marcos, R., Hernández, A., 2020. Biological effects, including oxidative stress and genotoxic damage, of polystyrene nanoparticles in different human hematopoietic cell lines. J. Hazard Mater. 398, 122900 https://doi.org/10.1016/j.jhazmat.2020.122900.

Schröter, L., Ventura, N., 2022. Nanoplastic toxicity: insights and challenges from experimental model systems. Small 18 (31), e2201680. https://doi.org/10.1002/smll.202201680.

Sears, W.M., Hunt, J.L., Stevens, J.R., 1981. Raman scattering from polymerizing styrene. 1 Vibrational-mode analysis. J. Chem. Phys. 75, 1589–1598. https://doi.org/10.1063/1.442262.

Sielecki, A.R., Fedorov, A.A., Boodhoo, A., Andreeva, N.S., James, M.N.G., 1990. Molecular and crystal-structures of monoclinic porcine pepsin refined at 1.8-a resolution. J. Mol. Biol. 214, 143–170. https://doi.org/10.1016/0022-2836(90)90153-D.

Stock, V., Fahrenson, C., Thuenemann, A., Dönmez, M.H., Voss, L., Böhmert, L., Braeuning, A., Lampen, A., Sieg, H., 2020. Impact of artificial digestion on the sizes and shapes of microplastic particles. Food Chem. Toxicol. 135, 111010 https://doi.org/10.1016/j.fct.2019.111010.

Tamargo, A., Molinero, N., Reinosa, J.J., Alcolea-Rodriguez, V., Portela, R., Bañares, M. A., Fernández, J.F., Moreno-Arribas, M.V., 2022. PET microplastics affect human gut microbiota communities during simulated gastrointestinal digestion, first evidence of plausible polymer biodegradation during human digestion. Sci. Rep. 12 (1), 528. https://doi.org/10.1038/s41598-021-04489-w.

Wright, S.L., Kelly, F.J., 2017. Plastic and human health: a micro issue? Environ. Sci. Technol. 51 (12), 6634–6647. https://doi.org/10.1021/acs.est.7b00423.

Xu, J.L., Lin, X., Wang, J.J., Gowen, A.A., 2022. A review of potential human health impacts of micro- and nanoplastics exposure. Sci. Total Environ. 851 (Pt-1), 158111 https://doi.org/10.1016/j.scitotenv.2022.158111.

Yong, C.Q.Y., Valiyaveettil, S., Tang, B.L., 2020. Toxicity of microplastics and nanoplastics in mammalian systems. Int. J. Environ. Res. Publ. Health 17 (5), 1509. https://doi.org/10.3390/ijerph17051509.

Zhang, Y.X., Wang, M., Yang, L., Pan, K., Miao, A.J., 2022. Bioaccumulation of differently-sized polystyrene nanoplastics by human lung and intestine cells. J. Hazard Mater. 439, 129585 https://doi.org/10.1016/j.jhazmat.2022.129585.